

A Point Process Model for Generating Biofilms with Realistic Microstructure and Rheology

J. A. STOTSKY, V. DUKIC, and D. M. BORTZ

Department of Applied Mathematics
University of Colorado
Boulder CO, 80309-0526
email: dmbortz@colorado.edu

November 24, 2021

Abstract

Biofilms are communities of bacteria that exhibit a multitude of multiscale biomechanical behaviors. Recent experimental advances have led to characterizations of these behaviors in terms of measurements of the viscoelastic moduli of biofilms grown in bioreactors and the fracture and fragmentation properties of biofilms. These properties are macroscale features of biofilms; however, a previous work by our group has shown that heterogeneous microscale features are critical in predicting biofilm rheology. In this paper we use tools from statistical physics to develop a generative statistical model of the positions of bacteria in biofilms. We show through simulation that the macroscopic mechanical properties of biofilms depend on the choice of microscale spatial model. Our key finding is that a biologically inspired model of the locations of bacteria in a biofilm is critical to the simulation of biofilms with realistic *in silico* mechanical properties and statistical characteristics.

1 Introduction

Biofilms are complex, multi-organism communities of bacteria. They are abundant in nature and grow readily in many industrial systems where they often cause maintenance and safety issues. Measures to mitigate or remove biofilms, though costly, are often necessary in the design and operation of many industrial systems [13, 17]. The demand for better biofilm control strategies and the causative role of biofilms in bacterial infections has inspired the development of numerous mathematical biofilm models [14, 17, 20, 28, 39, 42, 46, 51, 50, 52]. These models have been designed to capture a wide range of biofilm-related phenomena such as the biomechanical response to mechanical forces, growth dynamics, and persistence in the presence of antimicrobial substances. Yet, despite a thirty year history, it is only recently that the validation of models by comparison with empirical data has become a focus in computational biofilm studies. Recent works have shown agreement between experiment and simulation regarding the frequency dependent dynamic moduli [39], the ranges of certain spring constants [46], and the rate of disinfection of biofilms in response to antimicrobial substances [52]. However, this recent progress has also led to new questions.

Due to the complex behavior of biofilms, even state-of-the-art models rely on many assumptions. Material parameter values, biofilm morphology, and connectivity of biofilm networks are often specified heuristically, and even when parameters are informed by experimental results, there are difficulties. For instance, the experimental measurements of biofilm properties may differ by orders of magnitude between studies depending on the specifics of the conditions under which biofilms were grown and tested [34].

The assumptions noted before involve microstructural properties. Although, some microstructural properties have been measured [11, 38], little work has been done to elucidate the influence of microstructural properties on macroscale behaviors. Along these lines, there are two main goals to this paper. The first is to develop a microstructural description of *S. epidermidis* biofilms by estimating certain fundamental statistical

characteristics from experimental data. The second is to numerically demonstrate the efficacy of first and second order summary statistics for generating data with similar material properties as experimental data sets. The similarity of material properties is tested through simulation using the *heterogeneous rheology Immersed Boundary Method* (hrIBM) [20, 39].

This paper is organized as follows. In Section 2, we provide an overview of some non-parametric estimators of summary statistics of finite point processes. These estimators are based on those discussed in [40, 41, 31, 25]. We then apply these estimators to four data sets to compute the intensity, pair correlation function, and nearest neighbor distributions of each data set. The experimental data sets, obtained using the techniques described in [38, 34], consist of three dimensional coordinates of the centers of mass of approximately 4000 bacteria from live biofilms.

In Section 3, we introduce a statistical model for the arrangement of bacteria in a biofilm parametrized by the summary statistics discussed in Section 2. The model relies on results from the statistical physics of fluids and is designed to accurately replicate first and second order interactions between bacteria. From the model, an unnormalized probability density associated with the configuration of bacteria in the biofilm is obtained and used in Markov Chain Monte Carlo (MCMC) simulations to generate “artificial” biofilms [31, 49]. Unnormalized probability density functions are used due to the difficulty in computing the normalization constant needed to obtain a probability density of configurations. MCMC algorithms avoid dependence on normalizing constants since they only require ratios of probability densities.

In Section 4, we compare the material properties of the artificial biofilms generated by the statistical model presented in this paper, along with some previous biofilm generation models (e.g. [2, 42]), to data obtained through high resolution microscopy techniques. This comparison is achieved through simulations using the hrIBM to estimate the dynamic moduli of the resulting biofilms. In Section 5, we discuss the results, motivate some future research directions, and suggest potential improvements.

2 Summary Statistics of Point Data

In the spatial statistics literature, summary statistics such as the *number density* (commonly called the *intensity*), *pair correlation function*, and *nearest neighbor distributions* are frequently used to analyze random data. These summary statistics first appeared in diverse disciplines such as geography, forestry, and statistical physics; but have become more unified in recent years as the field of spatial statistics has evolved. Two dimensional estimates for these quantities are abundant [40, 45, 4, 16, 29, 15, 26, 35, 41], and three dimensional estimators, which are the focus of this work, have been applied to problems in astronomy and cosmology [10, 25]. In our discussion, we follow the notation of [41] and [31] where concise introductions to many of the quantities discussed here can be found. In Table 1 the most frequently used symbols are defined. In Appendices A.1 and A.2, we adapt optimization strategies from non-parametric density estimation to our estimates of the number density and pair correlation function.

Each realization of a point process is a random, countable set of distinct points in \mathbb{R}^3 , denoted by Φ . The restriction, $\Phi_W \equiv \Phi \cap W$, of the point process to a Borel set, W , containing the experimental data is of practical significance since experimental data is always contained in a bounded region. This restriction can lead to theoretical and numerical difficulties, and edge correction factors must often be derived in order to obtain accurate estimators of the statistical quantities of interest [40, 35, 23]. As will be shown in Sections 2.1, 2.2, 2.3, each statistic we compute from the data generally requires its own edge correction factor.

The experimental data available to us consists of sets of points in three dimensional space. Each point in a data set corresponds to the center of mass of an individual bacterium in a live biofilm. In Figure 1, we depict one of the four experimental data sets available to us. As indicated by the axes, the z coordinate of each data point will indicate its vertical location, and the x and y coordinates will indicate the horizontal location and depth of each point.

Although the complete statistical characterization of a point process is impractical, previous statistical studies show that information garnered from low order statistics of point processes is often sufficient to understand key features of data [4, 3, 29, 31, 41]. When plausible, models based on first and second order statistics are preferred since higher order statistics are difficult to estimate when only limited amounts of data are available and often are computationally expensive to compute when data is abundant. Thus, we proceed by estimating first and second order statistics of the biofilm data. In Section 4, we qualitatively

Table 1: Definitions of commonly used symbols. The n th order probability density when integrated over a product set, $B_1 \times B_2 \times \dots \times B_n$ gives the probability that for each \mathbf{r}_i , there exists a B_k such that $\mathbf{r}_i \in B_k$ for $i \in [1, n]$.

Symbol	Definition
W	Borel set containing experimental data
$\mathbf{r}, (x, y, z)$	point in \mathbb{R}^3
\mathbf{r}^n	collection of n points in \mathbb{R}^3
Φ	realization of a point process
$\Phi(B)$	number of points of Φ in set B
$\nu(B)$	Lebesgue measure of a set, B
$\rho^{(2)}(\mathbf{r}_1, \mathbf{r}_2)$	2nd order factorial moment density
$g^{(2)}(\mathbf{r}_1, \mathbf{r}_2)$	2nd order correlation function
$h^{(2)}(\mathbf{r}_1, \mathbf{r}_2)$	indirect correlation function, $h^{(2)} = g^{(2)} - 1$
$f^{(n)}(\mathbf{r}^n)$	n th order probability density
$\rho(\mathbf{r})$	number density (also known as the intensity), equivalent to $\rho^{(1)}(\mathbf{r})$
\hat{q}	estimator for quantity q
\tilde{q}	Hankel transform of quantity q
$\mathbb{E}[q]$	expectation of q
$k_b(r)$	smoothing kernel with support of radius b
$c_b(W)$	edge correction factor
$c(\mathbf{r}_1, \mathbf{r}_2)$	direct correlation function
$\phi(\mathbf{r})$	singlet potential
$v(\mathbf{r}_1, \mathbf{r}_2)$	pair potential
β	temperature
\mathbf{e}_x	unit vector in x -coordinate direction
$H_P(r)$	nearest-neighbor distribution function
G', G''	first and second dynamic moduli defined as $G' = (\sigma/\epsilon) \cos \delta$ and $G'' = (\sigma/\epsilon) \sin \delta$, where σ is a stress amplitude, ϵ a strain amplitude, and δ a phase lag (see [34])

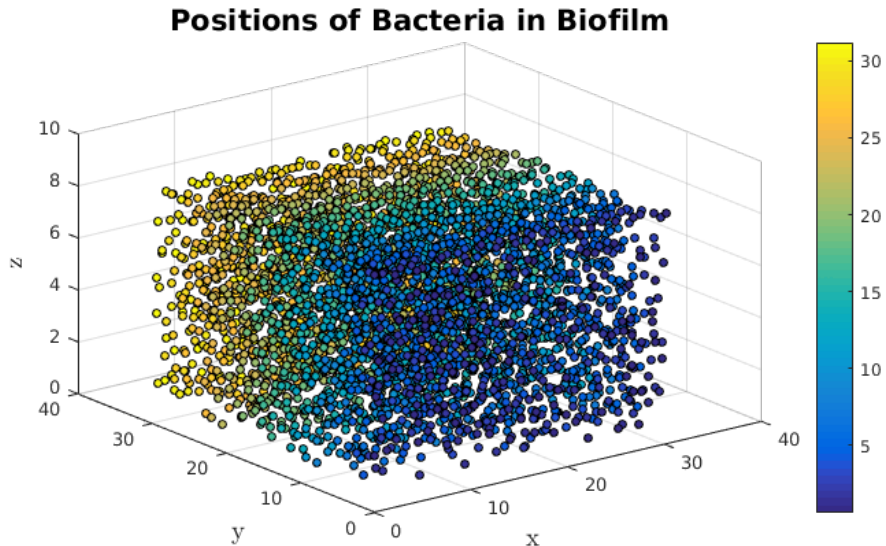


Figure 1: An experimental data set from a live biofilm. The data set is approximately $30\mu\text{m} \times 30\mu\text{m} \times 10\mu\text{m}$ in size and consists of the centers of mass of 3981 live bacteria. This data was obtained from high-resolution confocal microscopy images. The techniques used to obtain this data are discussed in [38]. The coloring is for ease of viewing and simply corresponds to the y coordinate of each bacterium.

validate the ability of first and second order statistics to characterize the arrangement of bacteria in *S. epidermidis* biofilms.

2.1 Point Process Number Density

To characterize the first order properties of a spatial point process, we ought to be able to estimate the average number of points in various subsets of the domain containing the data. In many cases, this average number of points is assumed simply to be proportional to the volume of the subset in consideration. However, a more accurate accounting of the first order properties of a points process requires the possibility of spatial variation.

For a general point process, under mild restrictions (see [9, §9.2]), the average number of points in some region, B , can be written as the Lebesgue integral of a function (known as a *rate*), $\rho(\mathbf{r})$,

$$\mathbb{E}[\Phi(B)] = \int_B \rho(\mathbf{r}) d\mathbf{r}.$$

This function, known as the *number density* or *intensity*, is of fundamental interest in the analysis of point processes. When presented with empirical point data, a typical goal is to infer whether the number density is constant, signifying a *stationary* point process, or spatially variable, indicating a *non-stationary* point process. To study the stationarity of a point process, an estimation procedure must be implemented to approximate the number density. When intuition about the nature of possible intensity variations is lacking, non-parametric estimators are often the tool of choice for the estimation of the number density. Since we are not aware of any previous models of the spatial statistics of bacteria in biofilms, a non-parametric density estimation is used in this work to allow for as much generality as possible.

In addition to being flexible, non-parametric estimates of the number density are often easy to implement and versatile, yielding suitable intensity approximations for many classes of point processes. However, a common source of concern with non-parametric estimates is the presence of statistical bias [36, 47, 19]. Non-parametric estimates are rarely pointwise unbiased¹, but are often asymptotically unbiased. Heuristically, the bias is due to inaccuracy in the numerical approximation of a Radon-Nikodym derivative [5] and is analogous to the truncation error associated with finite difference approximations of differentiable functions. Furthermore, as finite difference approximations depend on a spatial increment, non-parametric number density estimators are parametrized² by a scale parameter, b . Smaller values of b reduce the bias, but increase the variance of the estimator [33, 36, 47]. To ensure efficient estimators, careful selection of b is needed to balance this tradeoff between bias and variance. Further discussion of this balancing of bias and variance is included in the appendix.

2.1.1 Intensity Estimators

Our first approach was to examine the dependence of the intensity on the x , y , z individually (for instance, assume that $\rho(\mathbf{r}) = \rho(x)$, independent of y and z). With this approach, we found that although the bacteria locations are three dimensional coordinates, the number density is observed to vary only along the z -axis, with changes in the distance from the fluid-biofilm interface. As depicted in Figure 2a, it appears as though bacteria near the fluid-biofilm interface stratify into layers and pack more closely together than cells further interior. In Figure 2b, this phenomenon is clearly seen as bumps in the number density. To quantify this variation, we use an estimator based on the discussion in [41, §4]. Given a realization of a point process, the height dependent intensity is estimated by

$$\hat{\rho}(z) = \sum_{\mathbf{r}_i \in \Phi} \frac{k_b(\mathbf{r}_i \cdot \hat{\mathbf{e}}_z - z)}{c_{b,W}(z)} \quad (1)$$

¹This is similar in principle to non-parametric density estimation. A proof of the non-existence of pointwise unbiased estimators for probability density functions is given in [36]

²The term *non-parametric* refers to the absence of an underlying assumption about the functional form of $\rho(\mathbf{r})$, not the absence of any tuning parameters in the estimator. Aside from a few simple examples, non-parametric estimators almost always have some sort of parameter which must be chosen based on the scales of variation seen in the data.

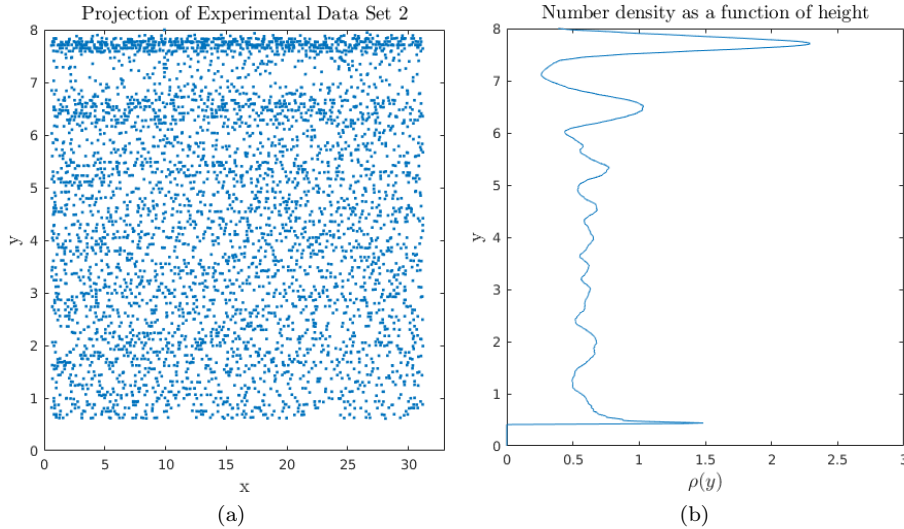


Figure 2: 2a: The projection of one of the data sets into the xz -plane is shown. The number density variation near the top of the domain can clearly be observed and some oscillatory intensity variation is discernible. 2b: The height dependent intensity, $\rho(y)$, from the same experimental data set is depicted. We used a scale parameter, $b = 0.2$ for all four data sets.

where $k_b(z) = (3/(4b)) \left(1 - (z/b)^2\right) \mathbf{1}_{|z| < b}$, is the *Epanechnikov kernel* [12], a commonly used density estimation kernel, with scale parameter, b . For notation, we use a hat (i.e. $\hat{\rho}$) to denote an estimator for a quantity. Defining A as the area of a cross-section perpendicular to the z -axis and W to be the domain containing the data, the denominator, $c_{b,W}(z)$ in Equation (1), is an edge correction factor defined as

$$c_{b,W}(z) = A \int_{[z-b, z+b] \cap W} k_b(z' + z) dz'.$$

The number density estimates obtained from data sets #1-4 exhibit some variation near the biofilm-fluid interface. Since the number of realizations (in our case, 4) is insufficient to propose a random intensity model, such as a Cox process model [9, §6.2], we parametrize our model on the intensity from a particular data set in each simulation in Section 3.

We also found that the precise form of the number density variation near the top of the biofilm did not have a substantial impact on the overall material properties of the biofilm. This was tested by conducting simulations in which the area of number density variation was removed from the data and observing that the difference in the strength of the biofilm (see Section 4) was not strongly effected.

As previously mentioned, the value of the scale parameter, b , has a significant impact on the resulting number density estimate and should be carefully chosen to balance variance and bias. If b is too small, the estimate will be noisy, whereas if b is too large, key features of the data will be blurred. The estimation of a one dimensional intensity function is quite similar to the non-parametric estimation of a probability density up to the normalization condition required of probability densities. This motivates the adaptation of the *Least Squares Cross-Validation* (LSCV) technique, a common optimization strategy for non-parametric probability density estimators [47], to optimize our choice for b in Equation (1). We refer the interested reader to Appendix A.1 for a discussion of LSCV bandwidth selection.

In addition to the number density, we will see in Section 3.2 that the gradient of the number density is also needed in the computation of a spatially dependent potential energy function. In order to compute this quantity, we adhere to the strategy discussed in [47] and use the differentiable, triweight kernel density estimator, defined as

$$T_b(z) = \frac{35}{32b} (1 - (z/b)^2)^3 \mathbf{1}_{\{|z| \leq b\}}.$$

Similar to the Epanechnikov kernel, the triweight kernel is a symmetric probability density function. However, it is more useful for density derivative estimation since it is twice differentiable whereas the Epanechnikov kernel is not differentiable. The number density derivative is approximated by

$$\hat{\rho}_z(z; b) = \frac{1}{A} \sum_{\mathbf{r}_i \in \Phi \cap W} \frac{\partial T_b(z - z_i)}{\partial z}.$$

As derivatives are more sensitive to noisy data, optimal balancing of variance and bias in number density derivative estimation tends to yield a larger value of b than that used in number density estimation [22]. By inspection of the resulting estimators, we found that a value of $b = 0.5$ seemed to give the best result. To correct for bias near the boundaries of the domain, adjustments to the kernel constructed by the technique in [23, Equation (8.2)] were used.

2.2 Pair Density and Pair Correlation Functions

The second order interactions of a spatial point process with nonzero number density can be characterized through either the *pair correlation function* (PCF) or the *second order factorial moment density* (SOFMD). Both functions measure the tendency of two points in space to be jointly contained in a realization of the point process. For two arbitrary points, \mathbf{r}_1 and \mathbf{r}_2 , the SOFMD, denoted by $\rho^{(2)}(\mathbf{r}_1, \mathbf{r}_2)$ is defined for any two sets, B_1 and B_2 , through the integral relation

$$\mathbb{E}[\Phi(B_1) \times \Phi(B_2)] = \mathbb{E}[\Phi(B_1 \cap B_2)] + \int_{B_2} \int_{B_1} \rho^{(2)}(\mathbf{r}_1, \mathbf{r}_2) d\mathbf{r}_1 d\mathbf{r}_2.$$

Note that for disjoint sets, the SOFMD is simply the expectation of the product of the number of points in each set. In fact, n th order factorial moment densities are defined for disjoint sets as

$$\mathbb{E}[\Phi(B_1) \cdot \Phi(B_2) \cdots \Phi(B_n)] = \int_{B_n} \cdots \int_{B_1} \rho^{(n)}(\mathbf{r}_1, \dots, \mathbf{r}_n) d\mathbf{r}_1 \cdots d\mathbf{r}_n.$$

For non-disjoint sets, the formulas for the factorial moment densities of arbitrary order are more complex and not listed here. However, there is some discussion in [41] of how such formulas may be derived.

The PCF, denoted $g^{(2)}(\mathbf{r}_1, \mathbf{r}_2)$, is defined as a rescaling of $\rho^{(2)}(\mathbf{r}_1, \mathbf{r}_2)$ by the number density,

$$g^{(2)}(\mathbf{r}_1, \mathbf{r}_2) = \frac{\rho^{(2)}(\mathbf{r}_1, \mathbf{r}_2)}{\rho(\mathbf{r}_1)\rho(\mathbf{r}_2)}.$$

For simplicity of notation, the superscript, (2), on $g^{(2)}(\mathbf{r}_1, \mathbf{r}_2)$ will be omitted except where there is ambiguity between $g^{(2)}$ and $g^{(n)}$ for some $n \neq 2$.³

The dependence of the PCF on its arguments can be simplified when the underlying point process is stationary or isotropic and stationary. For stationary point processes, the PCF is solely a function of $\mathbf{r}_1 - \mathbf{r}_2$ and, when the point process is also isotropic, it is further constrained to be dependent only on the radial distance, $|\mathbf{r}_1 - \mathbf{r}_2|$. When the number density is low enough (but nonzero) and the point process has a finite interaction radius, the PCF will tend towards one as $|\mathbf{r}_1 - \mathbf{r}_2| \rightarrow \infty$.

2.2.1 Pair Correlation Function Estimates

We would like to apply these simplifications since we are constrained by the finite size of the data sets. However, neither simplification mentioned above is directly applicable to point processes with variable intensity. In [4], the idea of a *second order intensity reweighted stationary* (SOIRS) point process is introduced. This idea is defined (assuming the intensity is nonzero) by considering the random measure

$$\Xi(B) = \sum_{\mathbf{x}_i \in \Phi \cap B} \frac{1}{\rho(\mathbf{x}_i)}.$$

³General n -point correlation functions that correspond to n th order *factorial moment densities* can be defined as

$$g^{(n)}(\mathbf{r}_1, \dots, \mathbf{r}_n) = \frac{\rho^{(n)}(\mathbf{r}_1, \dots, \mathbf{r}_n)}{\prod_{i=1}^n \rho^{(1)}(\mathbf{r}_i)}.$$

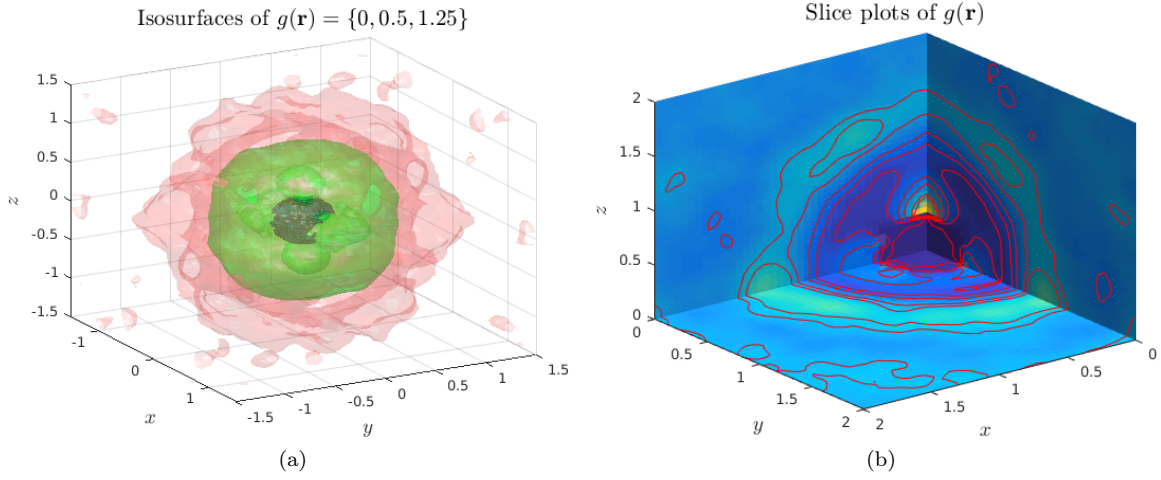


Figure 3: Both images are of PCFs averaged over the four experimental data sets. In Figure 3a: isosurfaces of the anisotropic pair correlation function at $g^{(2)}(\mathbf{r}) = 0$ (blue), 0.5 (green), and 1.25 (red) are depicted, and Figure 3b: contains slice plots and contours of the anisotropic pair correlation function. The anisotropic PCF is related to the isotropic PCF through the integral $g_i^{(2)}(r) = \frac{1}{4\pi} \int \int g_a^{(2)}(r, \phi, \theta) \sin \theta d\theta d\phi$. The anisotropic pair correlation function shows some vertical anisotropy, however most of the variation appears as a radially symmetric function.

If the second moment of Ξ is stationary, then the point process is deemed to be SOIRS. The advantage of such an assumption in our application, is that it allows for the approximation of a radially symmetric pair correlation of the form [4, 15]

$$\hat{g}(r) = \frac{1}{4\pi r^2 \bar{\gamma}_W(r)} \sum_{\substack{i \neq j \\ \{\mathbf{r}_i, \mathbf{r}_j\} \in \Phi \cap W}} \frac{k_b(r - |\mathbf{r}_i - \mathbf{r}_j|)}{\rho(\mathbf{r}_i)\rho(\mathbf{r}_j)}, \quad (2)$$

where $\bar{\gamma}_W(r)$ is the isotropized set covariance of W [41].

Such an assumption, if justified, is beneficial since it allows us to compensate for variable number density while allowing $g(\mathbf{r}_1, \mathbf{r}_2)$ to remain a radially symmetric function. Following [40], the expectation of $\hat{g}(r)$ is of the form :

$$\mathbb{E}[\hat{g}(r)] = \int g(|\mathbf{r}'|) k_b(|\mathbf{r}'| - r) d\mathbf{r}'. \quad (3)$$

Taking the limit as $b \rightarrow 0$ in Equation (3) shows that, under a few restraints on $k_b(r)$, $\hat{g}(r) \rightarrow g(r)$ at every point of continuity of $g(r)$. Thus, $\hat{g}(r)$ is asymptotically pointwise unbiased for continuous pair correlation functions. For discontinuous pair correlation functions, such as those arising from hard-sphere processes, the estimate is not asymptotically pointwise unbiased at the point of discontinuity, but is asymptotically convergent to $g(r)$ in the least squares sense.

In computing $\hat{g}(r)$, the estimator in Equation (2) is subject to an additional bias when $\rho(\mathbf{r})$ is approximated using the non-parametric estimator in Equation (1). In [4], it is shown that this source of bias can be reduced if the process is a Poisson process, and $\hat{\rho}(\mathbf{r})$ is altered when $\mathbf{r} \in \Phi$ such that,

$$\hat{\rho}(\mathbf{r}) = \sum_{\mathbf{r}_i \in \Phi \setminus \{\mathbf{r}\}} \frac{k_b(\mathbf{r} - \mathbf{r}_i)}{c_b(\mathbf{r})} = -\frac{k_b(0)}{c_b(\mathbf{r})} \mathbf{1}_{[\mathbf{r} \in \Phi]} + \sum_{\mathbf{r}_i \in \Phi} \frac{k_b(\mathbf{r} - \mathbf{r}_i)}{c_b(\mathbf{r})}.$$

For hard-sphere processes, the bias may also be reduced by this adjustment, but there is no longer a guaranteed improvement. This is because the bias that results from evaluating $\rho(\mathbf{r})$ at points of Φ can be positive or negative for hard-sphere processes, whereas it is always positive for Poisson processes.

In Figures 3a and 3b, an anisotropic and a radially symmetric estimate of $g(\mathbf{r})$ averaged over four data sets are depicted, and in Figure 4 the SOIRS radially symmetric PCF estimator defined in (2), computed from one data set, is depicted.

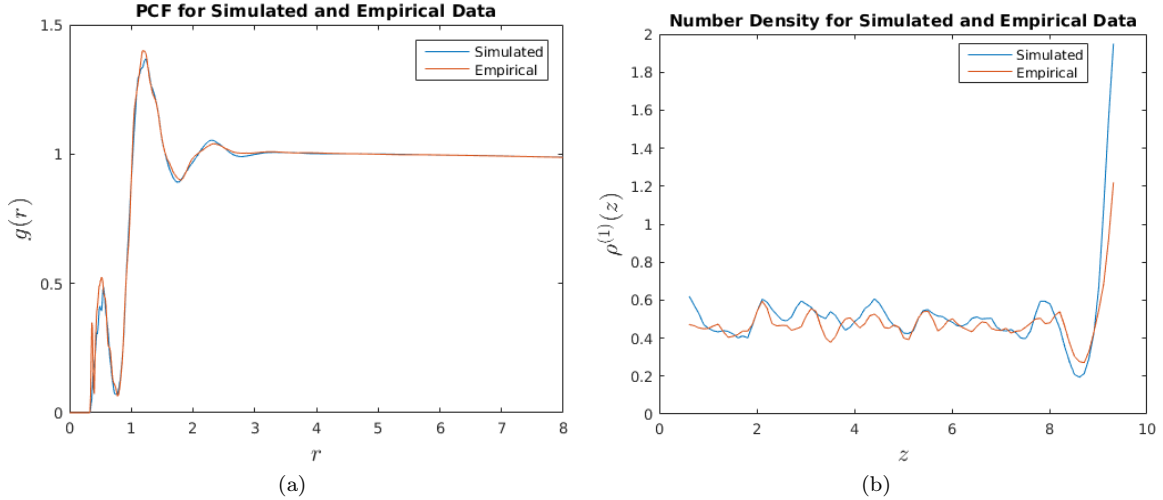


Figure 4: 4a: Comparison between experimental and simulated data of the SOIRS estimator for a radially symmetric pair correlation function. The radially symmetric pair correlation exhibits peaks at $r \approx 0.6$, $r \approx 1.2$, and $r \approx 2.4$ micrometers. The relative heights of the first two peaks is an interesting finding, and has been observed in biofilm data in a previous study [38]. The first, smaller peak is likely due to a small number of bacteria that were undergoing cellular division at the time the data set was recorded although the possibility of some experimental error cannot be definitively ruled out [37]. 4b: Comparison of number density between experimental data and simulated data. The simulation method used to generate data is discussed in Section 3.

An intriguing property of the biofilm data is the presence of two prominent peaks in the pair correlation function. It has been suggested that the first, smaller peak in Figure 3 is indicative of bacteria undergoing cell division at the time their position was measured [37]. The second peak occurs near the average diameter of a non-dividing bacterium. The third peak at $r \approx 2.4\mu m$ is indicative of regularity in the data [21, §5] and is likely the effect of more distant bacteria.

Recall from Figure 2 that there is evidence of variability in the number density along the z axis. This motivated our assumption of a SOIRS process in analyzing the data. However, we have not provided any evidence against an alternative hypothesis: that the PCF is not translation invariant. To make a convincing argument in favor of the SOIRS assumption (or at least that it is reasonable), it is necessary to estimate the magnitude of the variability of the pair correlation function.

To test for variability in the pair correlation function, its estimator, $\hat{g}(r)$ is calculated for various subsets of the full data set, $\Phi \cap W$. In particular, we compute $\hat{g}(r)$ over sets of the form $V_z = [z - \Delta z, z + \Delta z] \cap W$ with $z \in (\min(z_i), \max(z_i))$ where z_i are the z -coordinates of the bacteria, and $\Delta z = 1\mu m$. Computing $\hat{g}(r)$ on V_z as a function of z , we found only small variations in the resulting PCF. To fully utilize the available data in these computations, we use an altered estimator of $g(r)$, denoted $\hat{g}_{V_z}(r)$,

$$\hat{g}_{V_z}(r) = \frac{1}{4\pi r^2 \bar{\gamma}_{V_z, W}(r)} \sum_{\mathbf{r}_i \in V_z \cap \Phi} \sum_{\mathbf{r}_j \in W \cap \Phi \setminus \{\mathbf{r}_i\}} \frac{k_b(r - |\mathbf{r}_i - \mathbf{r}_j|)}{\rho(\mathbf{r}_i)\rho(\mathbf{r}_j)}$$

with

$$\bar{\gamma}_{V_z, W}(r) = \frac{1}{4\pi r^2} \int \nu(W \cap V_{z, t}) dt.$$

The integration is carried out over the surface of a sphere of radius r in \mathbb{R}^3 . This altered estimator is used since it takes into account data that is in W but not V_z in the inner summation. This reduces the truncation errors that could occur if we used the estimator in Equation (2). It is in essence a generalization of our standard PCF estimator to allow for the case that \mathbf{r}_i and \mathbf{r}_j correspond to different types of points (or points in different subdomains).

Upon computation, we note that the mean square error⁴ over z remained less than 0.05 for $r \in (0, 2)$. We do observe some variation with z in the pair correlation function, however, it seems to be a minor effect. In particular, we note that in some of the data sets, the height of the first peak in $\hat{g}(r)$ decreases from the bottom to the top of W . Although it would be ideal to compute a nonstationary estimate for $g(\mathbf{r}_1, \mathbf{r}_2)$, in practice, we found our calculations for such an estimator to be noisy, and unreliable for small values of $|\mathbf{r}_1 - \mathbf{r}_2|$ given the amount of data available. Thus, we have approximated the variable pair correlation function with a SOIRS form of $\hat{g}(r)$ for use in our computations.

As a final note, alternative approaches for estimating $g(r)$ by maximum likelihood estimation and Takacs-Fiksel estimation have been explored in several papers [3, 4, 31, 35]. With maximum likelihood estimation, the pair potential is assumed to be a member of a predetermined class of functions that differ through some set of parameters that can be optimized to fit the data. We did not proceed with this approach due to the unusual structure of the pair correlation function. With Takacs-Fiksel estimation, $g(r)$ is assumed to be a piecewise function (i.e. piecewise polynomial). The weights of the coefficients in the piecewise approximant are found by maximizing a nonlinear system of equations. Possible issues with such an approach here are the computational cost to accurately resolve $g(r)$ over a range of r and the attainment of a continuous (not just piecewise continuous) result.

2.3 Nearest Neighbor Distributions

Usually, direct numerical examination of the convergence in probability of point processes is impractical due to limitations on the amount of data available and the computational infeasibility of carrying out tests needed to fully assess convergence. Although generally insufficient to rigorously prove convergence, comparisons between summary statistics, may be used to provide evidence of similarities between point processes.

As will be discussed in subsequent sections, a statistical model designed to match the first and second order statistical properties of experimental data will be developed. Since lower order factorial product densities do not fully characterize a point process, the assumption that the data is well characterized by these statistics may be bolstered by comparisons of summary statistics that depend on statistical correlations of all orders. In this capacity, the k -nearest neighbor distributions are useful.

The k th-nearest neighbor distribution is defined as the probability density function of distances between a point $\mathbf{r} \in \Phi$ and the k th closest point $\mathbf{r}' \in \Phi \setminus \{\mathbf{r}\}$. Discussions about these distributions and their relation to moment densities can be found in [44] and [43].

Following [43, 44], the *nearest neighbor distribution function* (NNDF), is defined as the probability,

$$E_P^{(1)}(r) = \Pr \left[\min_{\mathbf{r}' \in \Phi \setminus \{\mathbf{r}\}} |\mathbf{r} - \mathbf{r}'| \leq r, \quad \mathbf{r}' \in \Phi \right].$$

The *nearest neighbor probability density* (NNPD), $H_P(r)$, defined as the derivative of $E_P(r)$ with respect to r , is often computed as well. The k th-nearest neighbor distributions are defined by

$$E_P^{(k)}(r) = \Pr \left[\min_{\{\mathbf{r}_1, \dots, \mathbf{r}_k\} \in \Phi \setminus \{\mathbf{r}'\}} \left(\max_{i=1..k} |\mathbf{r}_i - \mathbf{r}'| \right) \leq r, \quad \mathbf{r}' \in \Phi \right],$$

$$H_P^{(k)}(r) = \sum_{i=0}^{k-1} \left(\frac{\partial}{\partial r'} E_P^{(k)}(r') \right) \Big|_{r'=r}.$$

Along with the intensity and pair correlation function, we use the NNPDs as a means of comparing experimental data to realizations of point processes generated through simulation. As shown in [43, 44], $H_P^{(k)}(r)$ depends on relations of all orders between points in the point processes, not just the lower order summary statistics which can be estimated with the methods discussed in Section 2.2. Although equivalence in NNPDs does not guarantee equivalence of two point processes in probability, if two point processes are equal in probability, they must have the same nearest neighbor distributions. In practice, testing for equivalence in probability of a general point process is computationally infeasible, and would require an inordinate amount of data, however the nearest neighbor distributions are a useful summary statistic due to their low dimensionality, and the ease with which they can be estimated.

⁴the mean square error is defined as $E = \int_{r_0}^{r_1} (\hat{g}_{V_z}(r) - \hat{g}(r))^2 dr$. It is approximated by a trapezoid rule quadrature.

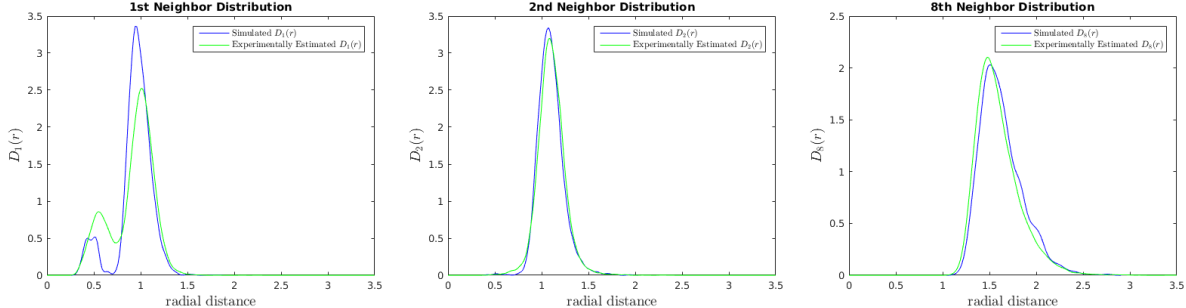


Figure 5: Comparison of nearest neighbor density functions between a simulated biofilm, and the experimental data. The bimodal behavior in the 1st neighbor distribution is not completely captured by the model, however, higher NNDFs (2 and 8 depicted here) are very accurately matched by the model.

Two disadvantages of nearest neighbor distributions as a means of comparing point processes are their lack of directional information, and that, as defined here, they are spatially homogeneous. Thus, the NNPDs we compute are best understood as homogenized variants of a more general nearest neighbor distribution that may depend on location. Since only four data sets are available, the computation of a spatially variable NNPD would be a formidable difficulty, and subject to greater variance than the homogenized NNPD.

2.3.1 Nearest Neighbor Distribution Estimators

To estimate the nearest neighbor distributions, we use *minus sampling* [41]. Minus sampling is the technique of constructing estimators that “leave out” points near the edges of the domain to mitigate edge effects. Minus sampling estimators are less efficient than other estimators because they do not utilize all available data. However, for statistics that are strongly influenced by edge effects, the benefit in reducing edge effects can be well worth the inefficient use of data. Using the symbol, \ominus , to denote Minkowski subtraction [41, §1], the nearest neighbor distribution is estimated as,

$$\hat{H}_P(r) = \frac{1}{\Phi(W \ominus \mathcal{B}_{r_c}(0))} \sum_{\mathbf{r}_i \in \Phi_W \ominus \mathcal{B}_{r_c}(0)} k_b \left(r - \left| \mathbf{r}_i - \arg \min_{\mathbf{r} \in \Phi \cap W \setminus \{\mathbf{r}_i\}} |\mathbf{r}_i - \mathbf{r}| \right| \right).$$

Minus sampling is suitable in our application since the box-shaped geometry of the domain dictates that most of the data is located away from the edges. Thus, the loss of data due to minus sampling is not severe. Even though there is a variation in number density near the top of the domain, we found that computations of the NNPDs that left out this portion of the data did not have a pronounced effect on the resulting estimate.

Because $H_P(r)$ is a one dimensional probability density, kernel density estimation methods of choosing b based on the cardinality of Φ_W are used [33, 36]. In particular, we use the *ksdensity* function in Matlab to compute $H_P(r)$ once r_c is known. To specify r_c , we first compute a preliminary estimate, $\hat{H}_{P,0}(r)$, without minus sampling (e.g. assuming $r_c = 0$), and then take r_c equal to the supremum,

$$r_c = \arg \sup_r \left\{ \hat{H}_{P,0}(r) > 0 \right\}.$$

This choice ensures that, with high probability, the nearest neighbor of each point of $\Phi_W \ominus \mathcal{B}_{r_c}(0)$ is contained in Φ_W . Specifically, the expected error is the probability $\Pr[\min_{\mathbf{r}_j \in \Phi} |\mathbf{r}_i - \mathbf{r}_j| > r_c, \mathbf{r}_i \in \Phi \ominus \mathcal{B}_{r_c}(0)]$. Since each data set contains ~ 4000 bacteria locations, this probability should be on the order of 10^{-3} . A second bias term arises from the use of non-parametric density estimators that have finite support for nonzero b . We expect this source of bias to be small since the asymptotic bias of kernel smoothing is typically $\mathcal{O}(n^{-4/5})$ [33] where n is size of the data set (~ 4000 for each biofilm data set). For $k > 1$, analogous estimators are used with r_c replaced by $r_c^{(k)} = \arg \sup_r \left\{ \hat{H}_{P,0}^{(k)}(r) > 0 \right\}$. For larger values of k , the minus sampling technique is expected to become inaccurate as the subset of W from which points may be chosen shrinks. However, we found that $r_c^{(k)}$ does not rapidly increase with k , and at least for $k \leq 20$, the amount of data that must be

disregarded due to minus sampling is small compared to the amount of data in each data set. In Figure 5 we show the nearest neighbor functions computed for the experimental data (averaged over four data sets) and a realization of a statistical model discussed in the next section.

3 Statistical Model for Bacterial Spatial Arrangement

In this section, we introduce a statistical model for the spatial arrangement of bacteria in biofilms, and discuss a method to generate realizations of the model. Our approach, inspired by results from the statistical physics of fluids [21], is to characterize the first and second order interactions between bacteria by the computation of empirical *pair potential* and *singlet energy* functions. These energy functions are related to the number density and pair correlation functions computed in Section 2 through an integral equation known as the *Ornstein-Zernike* (OZ) equation, a closure relation which provides a formula for the pair potential in terms of computable quantities, and a number density integral equation, derived in [30] for the singlet potential.

In our model, we apply a hypernetted-chain closure relation, and numerically solve the OZ and the number density integral equation to obtain the pair potential and singlet potential. Implicit in this approach is the assumption 1st and 2nd order statistics are sufficient to reconstruct the data. The resulting energy functions are then used to construct probability density functions.

In practice, it is difficult to determine the normalizing constant needed in the construction of the probability density function over configurations of points in the point process. To avoid this issue, we use the energy functions obtained from the model to construct unnormalized probability density functions. Realizations of the model can then be generated through simulation using a Markov chain Monte Carlo method (MCMC). The result of each simulation is a set of points in a domain, W , which have similar statistical properties, as measured by the tools discussed in Section 2, to the experimental data sets.

3.1 Pairwise Interaction Processes

For a general Markov point process [31, §6], the probability that a realization of the point process defined on a region, W , has some property, F , can be written as

$$\Pr(\Phi \in F) = \sum_{n=0}^{\infty} \frac{\exp(-\nu(W))}{n!} \underbrace{\int_W \dots \int_W}_n 1[\Phi \in F] f_n(\mathbf{r}_1, \mathbf{r}_2, \dots, \mathbf{r}_n) d\mathbf{r}_1 \dots d\mathbf{r}_n.$$

Each term, $f_n(\mathbf{r}_1, \dots, \mathbf{r}_k)$ is an n th order probability density function of the configuration of n points. It is defined as the conditional probability density given a realization of the point process containing n points, e.g. for an n -tuple of Borel sets, $\{B_1, \dots, B_n\}$,

$$\mathbb{E}[\mathbf{x}_1 \in B_1, \dots, \mathbf{x}_n \in B_n | \Phi(W) = n] = \int_{B_1} \dots \int_{B_n} f^{(n)}(\mathbf{r}_1, \dots, \mathbf{r}_n) d\mathbf{r}_1 \dots d\mathbf{r}_n.$$

If there are only first and second order interactions between points, the point process is known as a *pairwise interaction process*, and the n th order probability can be written following [21] and [31] as

$$f_n(\mathbf{r}_1, \dots, \mathbf{r}_n) = \frac{1}{Z_n} \exp \left[-\beta \sum_{i=1}^n \phi(\mathbf{r}_i) - \beta \sum_{i=1}^n \sum_{j=i+1}^n v(\mathbf{r}_i - \mathbf{r}_j) \right],$$

where $\phi(\mathbf{r})$ is the *singlet potential*, $v(\mathbf{r}_1, \mathbf{r}_2)$ is the *pair potential*, the normalizing constant, Z_k , is known as a configurational integral (closely related to a thermodynamic partition function) and, β is inversely proportional to the temperature. This is a vast simplification of the general Markov point process as pairwise interaction processes are specified by just two functions, $\beta\phi(\mathbf{r})$ and $\beta v(\mathbf{r}_1, \mathbf{r}_2)$. Assuming that the point process governing the bacteria positions is of this form, the next task is to estimate $\phi(\mathbf{r})$ and $v(\mathbf{r}_1, \mathbf{r}_2)$ from experimental data.

3.2 Computation of the Singlet and Pair Potentials

The computation of the pair correlation function given a pair energy function is a long standing and thoroughly studied problem in statistical mechanics, especially in the case of a homogeneous system [6, 27, 32]. The key components needed to solve this problem are the solution of the OZ equation, and the statement of a ‘‘closure-relation’’ that relates the pair energy to computable thermodynamic functions. The OZ equation, which can be derived through functional differentiation of the thermodynamic grand canonical ensemble, gives the definition of a correlation function, known as the *direct correlation function* (DCF), in terms of the PCF and the number density. This is important as the most successfully used closure relations are algebraic relations between the DCF, PCF, and pair potential. In contrast to the problem of using an assumed pair potential to obtain the PCF, here we discuss the numerical solution of the inhomogeneous inverse problem: the computation of a pair potential given a pair correlation function. Such inverse solutions of the OZ equation appear to have first been studied in [27], and numerical studies tend to favor Fourier methods to solve the relevant equations [24].

For a variable number density, $\rho(\mathbf{r})$, the OZ equation can be written as

$$h(\mathbf{r}_1, \mathbf{r}_2) = c(\mathbf{r}_1, \mathbf{r}_2) + \int \rho(\mathbf{r}_3) c(\mathbf{r}_1, \mathbf{r}_3) h(\mathbf{r}_2, \mathbf{r}_3) d\mathbf{r}_3. \quad (4)$$

The function, $h(\mathbf{r}_1, \mathbf{r}_2) \equiv g(\mathbf{r}_1, \mathbf{r}_2) - 1$, is known as the *indirect correlation function*, and $c(\mathbf{r}_1, \mathbf{r}_2)$ is the DCF. Equation (4) can be further simplified if, allowing for arbitrary variation in the z -direction, we assume that $h(\mathbf{r}_1, \mathbf{r}_2) = h(|\mathbf{r}_1 - \mathbf{r}_2|)$ is translation invariant and isotropic, and that $c(\mathbf{r}_1, \mathbf{r}_2)$ is radially dependent in the x and y coordinates. The assumption of a radially symmetric $h(r)$ is implied by the assumption of a SOIRS process. The assumption of radial symmetry in the horizontal plane is justified since it matches the observed variation in number density. It is also possible to show that, given a transversely isotropic pair correlation function, and vertically variable number density, the OZ equation admits transversely isotropic direct correlation functions. Defining $|\mathbf{r}|_{xy} = \sqrt{x^2 + y^2}$, and using the assumption of transverse anisotropy,

$$h(|\mathbf{r}_1 - \mathbf{r}_2|) = c(|\mathbf{r}_1 - \mathbf{r}_2|_{xy}, z_1, z_2) + \int \rho(z_3) c(|\mathbf{r}_2 - \mathbf{r}_3|_{xy}, z_2, z_3) h(|\mathbf{r}_1 - \mathbf{r}_3|) d\mathbf{r}_3. \quad (5)$$

Equation (5) can be written as a convolution over the xy plane, and an integration over the z plane. With $\hat{\mathbf{e}}_x$ and $\hat{\mathbf{e}}_y$ representing the Cartesian unit vectors in the x and y directions, setting $\mathbf{r}'_3 \cdot (\hat{\mathbf{e}}_x + \hat{\mathbf{e}}_y) \leftarrow (\mathbf{r}_3 - \mathbf{r}_2) \cdot (\hat{\mathbf{e}}_x + \hat{\mathbf{e}}_y)$, we obtain

$$h(|\mathbf{r}_1 - \mathbf{r}_2|) = c(|\mathbf{r}_1 - \mathbf{r}_2|_{xy}, z_1, z_2) + \int \int \int \rho(z_3) c(|(\mathbf{r}_1 - \mathbf{r}_2) - \mathbf{r}'_3|_{xy}, z_1, z_3) h(|\mathbf{r}'_3|) dx'_3 dy'_3 dz_3.$$

In order to determine the pair energy, a closure relation that defines $v(r_{12}, z_1, z_2)$ in terms of $g(|\mathbf{r}_1 - \mathbf{r}_2|)$ and $c(r_{12}, z_1, z_2)$ is required. We use the the hypernetted-chain (HNC) equation, given as

$$\beta v(r_{12}, z_1, z_2) = (h(|\mathbf{r}_1 - \mathbf{r}_2|) - c(r_{12}, z_1, z_2)) - \log g(|\mathbf{r}_1 - \mathbf{r}_2|).$$

In addition to the HNC, a separate closure relation, known as the Percus-Yevick (PY) closure is commonly applied. Both closure relations are approximate, and, depending on the situation, one closure may be more suitable than the other. In our case we chose to use the HNC as we found our numerical results to be more stable as compared with the PY equation, although for almost all values of r_{12}, z_1, z_2 , both the HNC and PY results were very similar. In Figure 6, the pair potential energy, obtained by applying the numerical methods described below to the OZ equation with a HNC closure, is depicted.

To complete the model, the singlet energy must be estimated. We use an equation that relates the number density and DCF to an external (or singlet) energy. This relation was originally derived in [30] to describe density variation at a fluid-vapor interface,

$$\beta \frac{\partial}{\partial z} \phi(z) = - \frac{\partial}{\partial z} \log \rho(z) + \int c(\mathbf{r} - \mathbf{r}', z', z) \frac{\partial}{\partial z'} \rho(z') d\mathbf{r}'. \quad (6)$$

Although derived for a different problem, we do not see anything in the derivation that makes the equations application to biofilm simulation invalid. After calculating the energy derivative, integration is done to

obtain the singlet energy. Upon integration, we set the constant of integration to 0 since only ratios of the form $e^{-\beta\phi(\mathbf{r}_1)}/e^{-\beta\phi(\mathbf{r}_2)}$ will be needed for simulations.

Because the number density is known from empirical estimates, Equation (5) can be solved independently of Equation (6). Thus, our approach is to first solve Equation (5) for $c(r_{12}, z_1, z_2)$, and then solve Equation (6) using $c(r_{12}, z_1, z_2)$ to obtain $\phi(z)$. As we have previously discussed the computation of $\rho(z)$ and $h(r_{12}, z_1, z_2)$ (see Section 2), it remains to devise a numerical solution method for Equations (5) and (6).

3.3 Numerical Solution to the Singlet and Pair Potential Equations

After obtaining estimates for $h(|\mathbf{r}_1 - \mathbf{r}_2|)$ and $\rho(z)$ using the methods of Section 2, Equations (5) and (6) must be solved numerically. In the homogeneous case, the integral term in the OZ equation becomes a convolution that can be efficiently and accurately handled by Fourier transform methods. However, due to the inhomogeneous number density, the integral over z is not a convolution in this present application. In fact, with a variable number density, the OZ equation implies that the pair correlation and direct correlation functions cannot both simultaneously be translation invariant. A proof of this fact is straightforward and shown in the Appendix. Thus the standard Fourier transform methods will not apply to our application.

As discussed in the previous section, to simplify Equation 4, we assume that the xy dependence of the pair correlation and direct correlation functions is homogeneous with regard to within-plane translations and is radially symmetric. This assumption makes the xy integration in Equation (5) a two dimensional radially symmetric convolution. The radially symmetric convolution of two functions can be found through use of the two dimensional Hankel transform, denoted $\mathcal{H}[\cdot]$, defined as the involutory transform

$$F(k) = \mathcal{H}[f(r)] = 2\pi \int_0^\infty J_0(2\pi kr) f(r) r dr$$

where $J_0(kr)$ is the 0th order Bessel J -function. The two dimensional Hankel transform can be applied to the OZ equation with $h(\mathbf{r}_1 - \mathbf{r}_2)$ and $r_{ij} = |(\mathbf{r}_i - \mathbf{r}_j) \cdot (\mathbf{e}_x + \mathbf{e}_y)|$ to obtain

$$\mathcal{H}[h](k, z_1, z_2) = \mathcal{H}[c](k, z_1, z_2) + \int \rho(z_3) \mathcal{H}[h](k, z_1, z_2) \mathcal{H}[c](k, z_1, z_3) dz_3.$$

In the discrete analog, we discretize z and r by setting $z_m = m\Delta z$, $m = 1, \dots, N$, and $r_\ell = j_\ell^{(0)} R / j_{N+1}^{(0)}$, where $j_\ell^{(0)}$ is the ℓ th root of the zeroth order Bessel J function, and R is the maximum value at which the estimator, \hat{h} from Equation (2) is computed. We set $R = 3\mu m$ since beyond this distance, the radially symmetric pair correlation function showed little variation. A discrete analogue of the Hankel transform is numerically computed in Matlab using the algorithm devised in [18] for each pair of z_m and z_n with $m, n \in [1, N]$.

Approximating the z -integral with the trapezoid method, the discrete approximation, $C_{k_\ell z_m z_n}^{(N)}$ of $\mathcal{H}[c](k_\ell, z_m, z_n)$ for each fixed value of k_ℓ and z_m , is found by solving

$$H_{k_\ell, z_m, z_n}^{(N)} = C_{k_\ell, z_m, z_n}^{(N)} + \sum_{n'=1}^N \hat{\rho}(n'\Delta z) H_{k_\ell, z_n, z_{n'}}^{(N)} C_{k_\ell, z_m, z_{n'}}^{(N)} \Delta z. \quad (7)$$

The symbol \sum'' indicates that the first and last term of the sum are halved. Equation (7) can be written as a matrix equation,

$$\mathbf{H}_{k_\ell, z_m}^{(N)} = (\mathcal{I}^{(N)} + \mathcal{M}_{k_\ell}^{(N)}) \mathbf{C}_{k_\ell, z_m}^{(N)} \quad \forall k_\ell, \forall z_m \quad (8)$$

where \mathcal{I} is the $N \times N$ identity matrix and,

$$\mathcal{M}_{k, ij}^{(N)} = \hat{\rho}(i\Delta z) H_{k, z_i, z_j}^{(N)} \Delta z.$$

In principle, the matrix $\mathcal{I} + \mathcal{M}$ could be ill-conditioned. However, in the simulations we conducted, the condition number of $\mathcal{I} + \mathcal{M}$ ranges only from 1 to 100. To verify that the error from matrix inversion does not become excessive, we compute the norm of $(\mathcal{I} + \mathcal{M}_{k_\ell})^{-1}$ in each solve. For an error \mathbf{e} in the estimation

of \mathbf{h} , the definition of the matrix norm ensures that $\|(\mathcal{I} + \mathcal{M}_{k_\ell})^{-1} \mathbf{e}\| \leq \|(\mathcal{I} + \mathcal{M}_{k_\ell})^{-1}\| \|\mathbf{e}\|$. Thus, as long as $\|(\mathcal{I} + \mathcal{M}_{k_\ell})^{-1}\|$ is not too large, the error will remain small. We also note that the trapezoid rule approximation is second order accurate, although this does not imply second order accuracy of the solution since it does not account for errors in the estimation of h by \hat{h} . We observed that the condition number is largest for $\ell < 5\Delta z$ ($\mathcal{O}(10^2)$ with the parameters we use), and decreases rapidly with increasing ℓ to $\mathcal{O}(1)$.⁵

Finally, after solving (8) for each value of ℓ and m , the Hankel transform can be applied to obtain $c_{r_\ell, z_m, z_n}^{(N)}$, the discrete approximation of $c(r_\ell, z_m, z_n)$. If there are N_r radial nodes, and N_z vertical nodes, $N_r N_z$ equations must be solved, and $2N_z^2$ transforms and inverse transforms must be computed. Although this leads to poor scaling, since we only need to compute the direct correlation function once, and can then store its value, the cost is not prohibitive, and, for the values of N_r and N_z we use, can be found in under a minute. In fact, the computation of $\hat{g}(r)$ is, by a substantial amount, the most time consuming step, followed by the discrete Hankel transformations of $h^{(N)}$ and $c^{(N)}$ for each z_m, z_n pair. The resulting pair potential for data set #3 is shown in Figure 6.

After computing $c^{(N)}$, a discrete approximation of the singlet energy now can be obtained. Discretizing Equation (6) with the trapezoid rule, and using the estimate, $c_{r_\ell, z_m, z_n}^{(N)}$, we arrive at an explicit approximation of $\phi'(z)$,

$$\beta\phi'_{z_n}{}^{(N)} = -\frac{1}{\hat{\rho}(n\Delta z)}\hat{\rho}'(n\Delta z) + 2\pi \sum_{m=1}^{N_z} \left(\sum_{\ell=1}^{N_r} c_{r_\ell, z_m, z_n}^{(N)} \Delta r_\ell \right) \hat{\rho}'(m\Delta z) \Delta z.$$

Given $\hat{\rho}'(z)$, the discretization should be second order accurate in Δz and Δr_ℓ . As with the estimation of $c(r_{12}, z_1, z_2)$, a rigorous error derivation must take into account error terms due to approximations used in estimating $\rho(z)$ by $\hat{\rho}(z)$ and $c(r_{12}, z_1, z_2)$ by $c_{r_\ell, z_m, z_n}^{(N)}$. For the approximation of $\phi(z)$, there is no advantage to using Hankel transforms for the radial integral since the real-space computation is explicit in $\phi(z)$. This differs from the pair energy computation where the real space integral equation is a three dimensional integral equation but, the transformed equation is a set of decoupled one dimensional integral equations. In that case, transforming in the r coordinate is highly beneficial. We also note that other numerical quadrature methods could be applied to compute the values of the integrals, however, we expect that the dominant error source is from the approximation of the pair correlation function and spatially variable number density. Thus, we do not expect significant differences resulting from different quadrature choices.

3.4 A Markov Chain Monte Carlo Algorithm

The pair energy function and singlet potential form the basis for an MCMC algorithm to generate “artificial” biofilms. The practical aspect of MCMC algorithms that makes them so useful is that they rely only on unnormalized probability densities. Given two realizations of a point process, denoted \mathbf{X}_1 and \mathbf{X}_2 , each containing n points in W , and an unnormalized probability density, $p^{(n)}(\mathbf{X}_1) \propto f^{(n)}(\mathbf{X}_1)$, the ratio

$$\frac{f^{(n)}(\mathbf{X}_1)}{f^{(n)}(\mathbf{X}_2)} = \frac{p^{(n)}(\mathbf{X}_1)}{p^{(n)}(\mathbf{X}_2)} = \frac{\exp \left[-\beta \sum_i \phi(\mathbf{r}_i^{(1)}) - \beta \sum_{i < j} v(\mathbf{r}_i^{(1)}, \mathbf{r}_j^{(1)}) \right]}{\exp \left[-\beta \sum_i \phi(\mathbf{r}_i^{(2)}) - \beta \sum_{i < j} v(\mathbf{r}_i^{(2)}, \mathbf{r}_j^{(2)}) \right]} \quad (9)$$

can be computed efficiently in comparison to evaluating or approximating the probability density, $f^{(n)}(\mathbf{X})$. If \mathbf{X}_2 differs from \mathbf{X}_1 by the location of only one point such that $\mathbf{r} \in \mathbf{X}_1$ and $\mathbf{r}' \in \mathbf{X}_2$, then (9) simplifies and can be computed in $\mathcal{O}(n)$ operations as

$$\frac{f^{(n)}(\mathbf{X}_1)}{f^{(n)}(\mathbf{X}_2)} = \exp \left[-\beta(\phi(\mathbf{r}') - \phi(\mathbf{r})) - \beta \sum_{i=1}^n v(\mathbf{r}_i, \mathbf{r}) + \beta \sum_{i=1}^n v(\mathbf{r}_i, \mathbf{r}') \right]. \quad (10)$$

Because $\phi(\mathbf{r})$ and $v(\mathbf{r}_1, \mathbf{r}_2)$ are computed using the methods of Section 3.3 on a grid and are not known analytically, interpolation is used to approximate their values at the points, $\mathbf{r}_i \in \Phi$, which are arbitrary points in space. Linear interpolation was the chosen interpolation method because it is computationally inexpensive and accurate in our case since the grid of points on which the energy is computed on in the

⁵The matrix norm used here is the 2-norm. This norm is also used in the computation of the condition number.

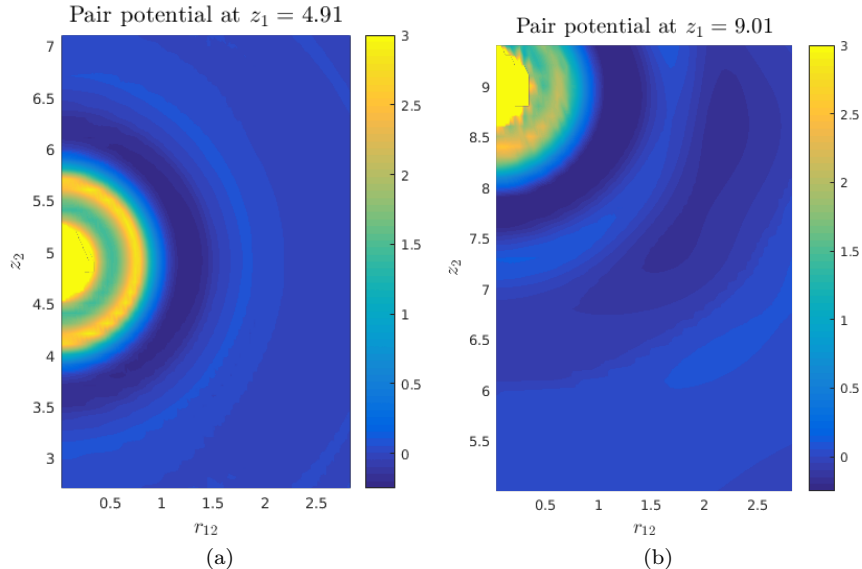


Figure 6: The potential, $v(r_{12}, z_1, z_2)$ as it is computed from the hypernetted-chain equation. The two subfigures show $v(r_{12}, z_1, z_2)$ for two different values of z_1 . Although the pair potential at both values is similar, they are not equivalent; the peaks and valleys in the pair correlation in 6b are slightly more pronounced than in 6a. The differences in the pair potential at different heights influences the height-dependent number density trends we observed in the biofilm data.

previous section has a small spatial step. Potential improvements could apply the ideas in [7] obtain MCMC chains such that have reduced dependence on the choice of interpolation method. For boundary conditions, we imposed periodicity in the two horizontal directions, and an impenetrable boundary at the top and bottom of the domain. Given $f^{(n)}$ (or $p^{(n)}$), the MCMC algorithm proceeds with the steps detailed in Algorithm 1.

In step 5 of Algorithm 1, a halting criterion must be used to determine whether to continue looping through steps 2-5 or to exit. Such criteria are usually based on easily computable quantities such as the total unnormalized density, $p^{(n)}(\mathbf{X})$, or, a characteristic such as the empirical pair correlation function [31, §8]. In our case, we observed that, with an update step drawn from a uniform distribution, $\delta\mathbf{X} \propto U([-1/2, 1/2]^3)$, the total energy leveled off after $\mathcal{O}(10^5)$ steps, and the average number of acceptances was approximately 1/2 the number of attempts. The computed value of $g(r)$ for each sample also stabilized by this point in each case. Thus, as a halting criterion, we compute the total energy of the sample every 10000 steps and stop after it has leveled off. In practice, this lead to convergence within 500000 steps in each simulation that we conducted.

The convergence in total energy of one particular realization is shown in Figure 7. There is a clearly distinguishable initial period of decreasing energy followed by a valley where the energy remains within a small range.

The algorithm is conditional on n , however, for large values of n , it has been observed that the difference between grand canonical and canonical MCMC results is small [31, §8]. If desired, it seems possible to augment the algorithm to include addition and deletion steps or to allow n to be a random variable in step 1 of the algorithm to obtain an unconditional method. However, such extensions also require knowledge of the distribution of n over distinct samples. Since we only have four experimental data sets, it seems unjustified to assume a distribution for n without more information.

4 Comparison of Material Properties

Although experimental results on biofilms often range drastically between different studies, it is generally agreed that over short time scales and moderate mechanical stresses, biofilms behave as viscoelastic materials [34]. One way to characterize biofilm rheology is through measurement of the dynamic moduli, which are

Algorithm 1 MCMC algorithm for generating realizations of a point process with spatial characteristics similar to those of the experimental data, conditioned on a known domain, W , of finite size. As a convergence criterion, we use the total unnormalized energy, which we observed to level off after $\mathcal{O}(10^5)$ update steps with an acceptance rate near 50%.

- 1: Generate n randomly placed points in a window, W . Denote this set of points \mathbf{X}_0 .
- 2: Displace one point, $\mathbf{x}_i \in \mathbf{X}_k$, chosen at random, by a uniformly random displacement, $\delta\mathbf{x}$ and set

$$\tilde{\mathbf{X}} = \{(\mathbf{X}_k \setminus \{\mathbf{x}_i\}) \cup \{\mathbf{x}_i + \delta\mathbf{x}\}\}.$$

- 3: Compute

$$\alpha = \min\left(\frac{f^{(n)}(\tilde{\mathbf{X}})}{f^{(n)}(\mathbf{X}_k)}, 1\right)$$

according to Equation (10) using interpolation as needed.

- 4: If $\tilde{\mathbf{X}} \subset W$, then with probability α , set $\mathbf{X}_{k+1} = \tilde{\mathbf{X}}$. Otherwise repeat steps 2-4.
 - 5: Set $k \leftarrow k + 1$ and repeat steps 2-4 unless a *convergence criterion* has been reached. If a convergence criterion has been reached, output \mathbf{X}_{k+1} and exit.
-

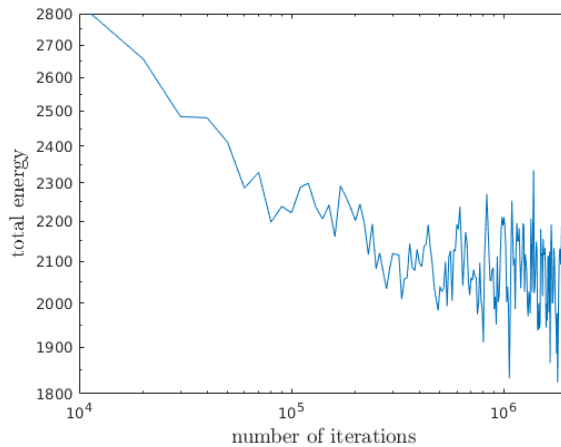


Figure 7: Convergence in the total energy, $E = \exp\left[-\beta \sum_i z(\mathbf{r}_i) - \beta \sum_{i < j} v(\mathbf{r}_i, \mathbf{r}_j)\right]$ of the MCMC method described here. The result here is plotted on a log-log scale to highlight the initial “burn-in” phase followed by the attainment of an “equilibrium” energy. The energy is plotted at every 10000th iteration. Even after the burn-in phases, there is still variability in the energy between iterations, but there is no downward trend in the energy.

defined in Table 1.

In Figure 8, we depict the dynamic moduli, for four different types of point processes and the experimental data. Since we have four experimental data sets available to us, we repeat the comparison for each data set. The “random” data sets are realizations of a Poisson process of constant number density, equal to the average number density of the experimental data sets. The “model” data is based on realizations of the model in Section 3, the grid-aligned data use a regular grid of points in simulation, and the grid-aligned plus perturbation uses the same grid-aligned data with an added perturbation drawn from a normal distribution of mean 0.

We see that the uniformly random and PCF models perform better than a grid aligned approximation, although some amount of improvement is seen when the grid aligned data is randomly perturbed. In each case, the comparisons are made between point processes with approximately the same number of points as the experimental data. (In the uniformly random, and model based simulations, the number of points is exactly the same as the experimental data)

To estimate the variability in the material properties for each of the point processes we have mentioned, the dynamic moduli are computed over 5 trials. Although it would be beneficial to observe a larger number of trials over a range of frequencies, the computational cost of such an endeavor is currently prohibitive.

5 Discussion

The results in Section 4 show how different models of the positions of bacteria in a biofilm can influence the mechanical properties of the simulated biofilm. It was found that the Poisson process model, and grid-aligned model do not yield results that are consistent with statistical characteristics of the experimental data. However, we were surprised to find that despite this difference from the experimental data, the Poisson model does lead to biofilms with similar dynamic moduli, performing as well as our model in terms of recreating the mechanical properties of a biofilm. In contrast, the grid-aligned model, as shown in Figure 8 is not a close match. These findings indicate that nonuniformity can lead to stronger biofilms in comparison to the grid-aligned case. We also show that the model introduced in Section 3, with first and second order characteristics informed by experimental data, yields agreement in the material properties and agreement in statistical properties of the data.

Although the uniformly random model exhibits similar dynamic moduli as experimental data, from a physical interpretation, it is clear that the bacteria positions cannot conform to a Poisson process. The lack of correlations between point locations, a defining feature of Poisson processes, implies that for any radius, r , there is a nonzero probability that within a given realization, two points of the process are separated by a distance less than r . In contrast, bacteria have finite radii and are impenetrable, thus the centers of mass of two bacteria cannot be separated by less than some hard-sphere radius. The hard-sphere property of the experimental data is readily apparent upon computation of the nearest neighbor distribution and the pair correlation function.

In contrast to our observations, we note that in [48], the network topology of an immersed boundary method model was not observed to have strong effects on bulk viscoelastic properties of the system. However, we believe that this difference is due to the magnitude of the number density of the point process being simulated and the average connectivity of each point. We choose a connectivity model with an average connectivity of close to 9 connections per bacteria, whereas [48] used a regular network of points with 27 linkages per node. It is our conjecture that at high number densities, and high levels of connectivity, the spatial positioning has less of an impact on rheological features, whereas for lower density and lower connectivity situations, the spatial positioning has a stronger effect. In a future work we plan to further study this idea.

In this paper, the focus was solely on the spatial arrangement of the centers of mass of bacteria. No attention was given to developing the “network” or clustering statistics of bacteria, i.e. what is the chance that two bacteria whose separation is \mathbf{r} are connected by viscoelastic links, and how strong is such a link expected to be? The reason for this omission is that current state of the art experiments allow for determination of bacteria locations, but to the extent of our knowledge, the connectivity of bacteria in a biofilm has not been experimentally measured. Thus, we use a simple distance based connectivity rule, assuming that bacteria within a certain radius are connected by a spring which cannot bend, as was originally proposed in [2], and

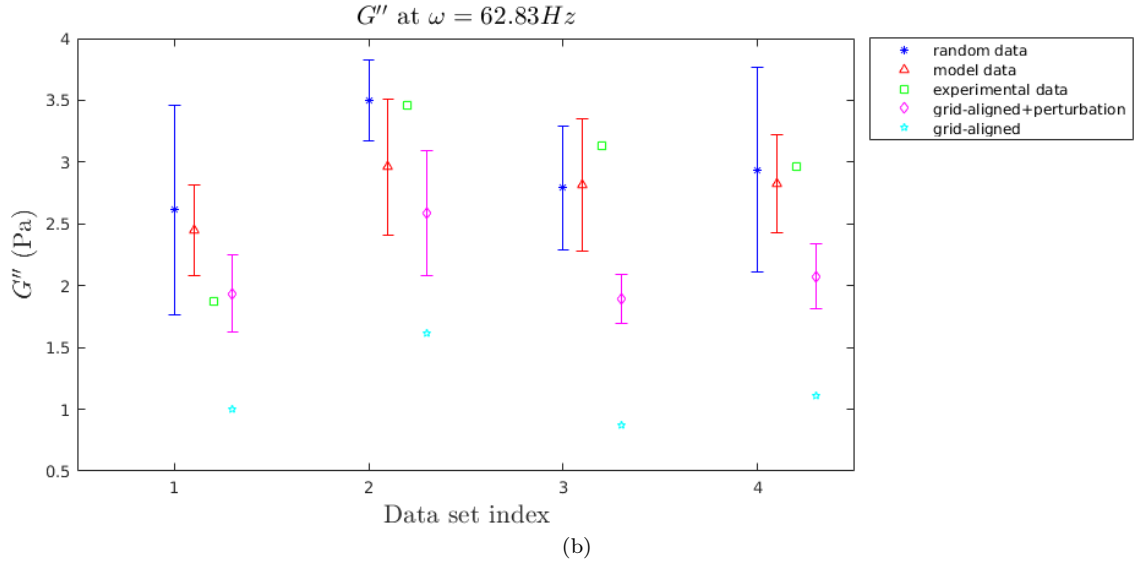
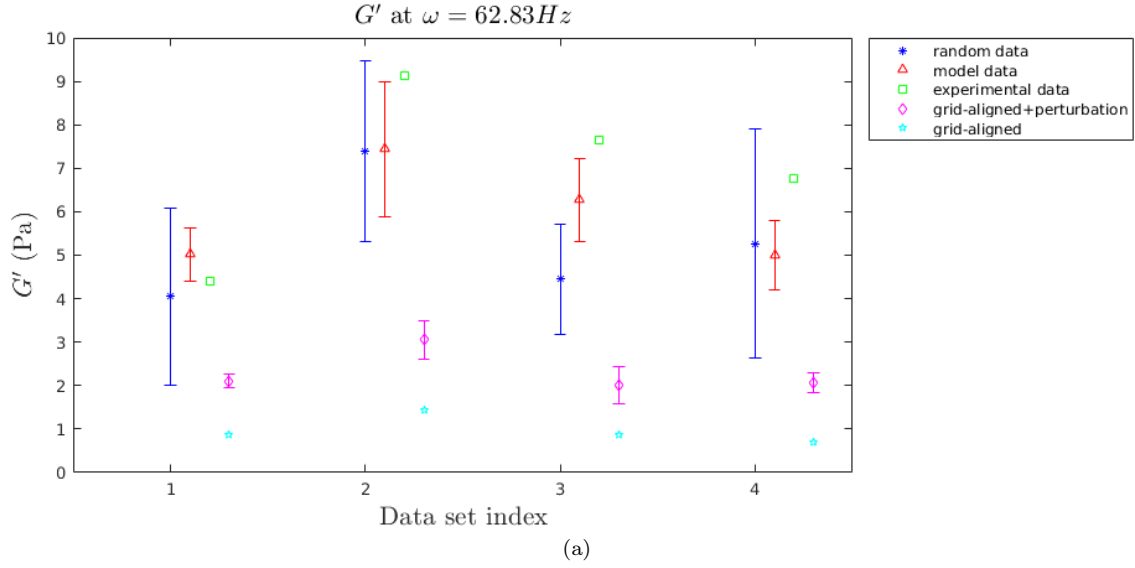


Figure 8: Figure 8a shows the comparison between the statistical models and the experimental data for G' and Figure 8b shows the the comparison for G'' . Both figures are from simulations at $\omega = 62.83Hz$. For the grid aligned data, the data falls on regular grid of the form $\mathbf{X} = (ih, jh, kh)$, for i, j, k being integers. For the Random Data and PCF Model, each entry corresponds to the average of 5 samples containing the same number of points and domain as each of four experimental data sets. For the grid aligned plus perturbation, the results are from five trials with the grid aligned data and a peturbation drawn from a normal distribution of mean 0 and deviation of 0.2. The x axis numbering corresponds to each of the four data sets the statistical models were designed to compare with. Error bars in Figure 8 are 95% confidence intervals. These are computed using Matlab's *normfit* function.

used again in [20] and [39]. Although this model is simple it yields realistic results when combined with appropriate viscoelastic models of the linkages. However, a more realistic connectivity model might impact the observed material properties. It would also be of interest to determine a mechanism by which springs can be ruptured due to the accumulation of stress such as in [42].

Although not the focus of our work, an interesting result that arose in the course of this study was the observation of oscillations in the number density of bacteria near the fluid-biofilm interface. It would be interesting to discover whether this variation in number density is a passive effect due to fluid motion at the biofilm-fluid surface or other experimental conditions, or whether it is a strategy employed by biofilm forming bacteria to improve the biological fitness of a given biofilm.

6 Acknowledgments

This work was supported in part by the National Science Foundation grants PHY-0940991 and DMS-1225878 to DMB, and by the Department of Energy through the Computational Science Graduate Fellowship program, DE-FG02-97ER25308, to JAS. The authors would also like to thank Mike Solomon (University of Michigan) and John Younger (Akadeum Life Sciences) for insightful discussions and suggestions concerning this work.

References

- [1] Abramson, I. S. (1982) On bandwidth variation in kernel estimates—a square root law. *The annals of Statistics*, 1217–1223.
- [2] Alpkvist, E. and Klapper, I. (2007) Description of mechanical response including detachment using a novel particle model of biofilm/flow interaction. *Water Science and Technology*, 55(8-9):265–273.
- [3] Baddeley, A. and Turner, R. (2000) Practical maximum pseudolikelihood for spatial point patterns. *Australian & New Zealand Journal of Statistics*, 42(3):283–322.
- [4] Baddeley, A. J., Møller, J., and Waagepetersen, R. (2000) Non- and semi-parametric estimation of interaction in inhomogeneous point patterns. *Statistica Neerlandica*, 54(3):329–350.
- [5] Billingsley, P. (2008) *Probability and measure*. John Wiley & Sons.
- [6] Blum, L. and Stell, G. (1976) Solution of Ornstein-Zernike equation for wall-particle distribution function. *Journal of Statistical Physics*, 15(6):439–449.
- [7] Conrad, P. R., Marzouk, Y. M., Pillai, N. S., and Smith, A. (2016) Accelerating asymptotically exact mcmc for computationally intensive models via local approximations. *Journal of the American Statistical Association*, 111(516):1591–1607.
- [8] Cronie, O. and van Lieshout, M. (2016) Bandwidth selection for kernel estimators of the spatial intensity function. *arXiv preprint arXiv:1611.10221*.
- [9] Daley, D. J. and Vere-Jones, D. (2007) *An introduction to the theory of point processes: volume II: general theory and structure*. Springer Science & Business Media.
- [10] Davis, M. and Peebles, P. (1983) A survey of galaxy redshifts. v—the two-point position and velocity correlations. *The Astrophysical Journal*, 267:465–482.
- [11] Dzul, S. P., Thornton, M. M., Hohne, D. N., Stewart, E. J., Shah, A. A., Bortz, D. M., Solomon, M. J., and Younger, J. G. (2011) Contribution of the *Klebsiella pneumoniae* capsule to bacterial aggregate and biofilm microstructures. *Applied and environmental microbiology*, 77(5):1777–1782.
- [12] Epanechnikov, V. A. (1969) Non-parametric estimation of a multivariate probability density. *Theory of Probability & Its Applications*, 14(1):153–158.

- [13] Flemming, H.-C. (2011) Microbial biofouling: unsolved problems, insufficient approaches, and possible solutions. In *Biofilm highlights*, 81–109. Springer.
- [14] Gaboriaud, F., Gee, M. L., Strugnell, R., and Duval, J. F. L. (2008) Coupled electrostatic, hydrodynamic, and mechanical properties of bacterial interfaces in aqueous media. *Langmuir*, 24(19):10988–10995.
- [15] Guan, Y. (2007) A least-squares cross-validation bandwidth selection approach in pair correlation function estimations. *Statistics & Probability Letters*, 77(18):1722–1729.
- [16] Guan, Y. (2008) On consistent nonparametric intensity estimation for inhomogeneous spatial point processes. *Journal of the American Statistical Association*, 103(483):1238–1247.
- [17] Guélon, T., Mathias, J.-D., and Stoodley, P. (2011) Advances in biofilm mechanics. In *Biofilm Highlights*, 111–139. Springer.
- [18] Guizar-Sicairos, M. and Gutiérrez-Vega, J. C. (2004) Computation of quasi-discrete hankel transforms of integer order for propagating optical wave fields. *JOSA A*, 21(1):53–58.
- [19] Hall, P. and Marron, J. S. (1991) Local minima in cross-validation functions. *Journal of the Royal Statistical Society. Series B (Methodological)*, 245–252.
- [20] Hammond, J., Stewart, E., Younger, J., Solomon, M., and Bortz, D. (2014) Variable viscosity and density biofilm simulations using an immersed boundary method, part i: Numerical scheme and convergence results. *CMES - Computer Modeling in Engineering and Sciences*, 98(3):295–340.
- [21] Hansen, J.-P. and McDonald, I. R. (1990) *Theory of simple liquids*. Elsevier.
- [22] Hardle, W., Marron, J., and Wand, M. (1990) Bandwidth choice for density derivatives. *Journal of the Royal Statistical Society. Series B (Methodological)*, 223–232.
- [23] Jones, M. C. (1993) Simple boundary correction for kernel density estimation. *Statistics and Computing*, 3(3):135–146.
- [24] Kelley, C. and Pettitt, B. M. (2004) A fast solver for the Ornstein–Zernike equations. *Journal of Computational Physics*, 197(2):491–501.
- [25] Kerscher, M., Szapudi, I., and Szalay, A. S. (2000) A comparison of estimators for the two-point correlation function. *The Astrophysical Journal Letters*, 535(1):L13.
- [26] Kolaczyk, E. D. and Dixon, D. D. (2000) Nonparametric estimation of intensity maps using Haar wavelets and Poisson noise characteristics. *The Astrophysical Journal*, 534(1):490–505.
- [27] Kunkin, W. and Frisch, H. L. (1969) Inverse problem in classical statistical mechanics. *Phys. Rev.*, 177:282–287.
- [28] Laspidou, C. S. and Rittmann, B. E. (2004) Modeling the development of biofilm density including active bacteria, inert biomass, and extracellular polymeric substances. *Water Research*, 38(14):3349–3361.
- [29] Lieshout, M. v. and Baddeley, A. (1996) A nonparametric measure of spatial interaction in point patterns. *Statistica Neerlandica*, 50(3):344–361.
- [30] Lovett, R., Mou, C., and Buff, F. (1976) The structure of the liquid-vapor interface. *J. chem. Phys.*, 65:2377.
- [31] Moller, J. and Waagepetersen, R. P. (2003) *Statistical inference and simulation for spatial point processes*. CRC Press.
- [32] Ornstein, L. and Zernike, F. (1914) The influence of accidental deviations of density on the equation of state. *Koninklijke Nederlandsche Akademie van Wetenschappen Proceedings*, 19(2):1312–1315.

- [33] Parzen, E. (1962) On estimation of a probability density function and mode. *The annals of mathematical statistics*, 33(3):1065–1076.
- [34] Pavlovsky, L., Younger, J. G., and Solomon, M. J. (2013) In situ rheology of *Staphylococcus epidermidis* bacterial biofilms. *Soft matter*, 9(1):122–131.
- [35] Ripley, B. D. (1991) *Statistical inference for spatial processes*. Cambridge university press.
- [36] Rosenblatt, M. et al. (1956) Remarks on some nonparametric estimates of a density function. *The Annals of Mathematical Statistics*, 27(3):832–837.
- [37] Stewart, E. J., Ganesan, M., Younger, J. G., and Solomon, M. J. (2015) Artificial biofilms establish the role of matrix interactions in *Staphylococcal* biofilm assembly and disassembly. *Scientific reports*, 5.
- [38] Stewart, E. J., Satorius, A. E., Younger, J. G., and Solomon, M. J. (2013) Role of environmental and antibiotic stress on *Staphylococcus epidermidis* biofilm microstructure. *Langmuir*, 29(23):7017–7024.
- [39] Stotsky, J., Hammond, J., Pavlovsky, L., Stewart, E., Younger, J., Solomon, M., and Bortz, D. (2016) Variable viscosity and density biofilm simulations using an immersed boundary method, part ii: Experimental validation and the heterogeneous rheology-ibm. *Journal of Computational Physics*, 317:204–222.
- [40] Stoyan, D., Bertram, U., and Wendrock, H. (1993) Estimation variances for estimators of product densities and pair correlation functions of planar point processes. *Annals of the Institute of Statistical Mathematics*, 45(2):211–221.
- [41] Stoyan, D., Kendall, W., and Mecke, J. (1995) Stochastic geometry and its applications. 1995. *Akademie-Verlag, Berlin*.
- [42] Sudarsan, R., Ghosh, S., Stockie, J. M., and Eberl, H. J. (2015) Simulating biofilm deformation and detachment with the immersed boundary method. *arXiv preprint arXiv:1501.07221*.
- [43] Torquato, S. (2013) *Random heterogeneous materials: microstructure and macroscopic properties*, volume 16. Springer Science & Business Media.
- [44] Truskett, T. M., Torquato, S., and Debenedetti, P. G. (1998) Density fluctuations in many-body systems. *Physical Review E*, 58(6):7369.
- [45] Van Lieshout, M. (2011) A J-function for inhomogeneous point processes. *Statistica Neerlandica*, 65(2):183–201.
- [46] Vo, G. D., Brindle, E., and Heys, J. (2010) An experimentally validated immersed boundary model of fluid–biofilm interaction. *Water Science and Technology*, 61(12):3033–3040.
- [47] Wand, M. P. and Jones, M. C. (1993) Comparison of smoothing parameterizations in bivariate kernel density estimation. *Journal of the American Statistical Association*, 88(422):520–528.
- [48] Wróbel, J. K., Cortez, R., and Fauci, L. (2014) Modeling viscoelastic networks in stokes flow. *Physics of Fluids (1994-present)*, 26(11):113102.
- [49] Yeong, C. and Torquato, S. (1998) Reconstructing random media. *Physical Review E*, 57(1):495.
- [50] Zhang, T., Cogan, N., and Wang, Q. (2008) Phase field models for biofilms. ii. 2-d numerical simulations of biofilm-flow interaction. *Commun. Comput. Phys*, 4(1):72–101.
- [51] Zhang, T., Cogan, N. G., and Wang, Q. (2008) Phase field models for biofilms. i. theory and one-dimensional simulations. *SIAM Journal on Applied Mathematics*, 69(3):641–669.
- [52] Zhao, J., Shen, Y., Haapasalo, M., Wang, Z., and Wang, Q. (2016) A 3d numerical study of antimicrobial persistence in heterogeneous multi-species biofilms. *Journal of theoretical biology*, 392:83–98.

A

A.1 Bandwidth Selection for the Estimation of the Number Density

In Section 3, it was necessary to estimate the number density of biofilms samples. In order complete this task, we used a kernel density based estimator of the form

$$\hat{\rho}(z; b) = \frac{1}{A} \sum_{\mathbf{r}_i \in \Phi \cap W} \frac{k_b(z - \hat{\mathbf{e}}_z \cdot \mathbf{r}_i)}{c(z; b)}.$$

As is typical with kernel density estimation, a choice of the scale parameter, b , must be made. Several typical techniques are discussed in [47]. The general idea is to minimize the *mean integrated square error* (MISE),

$$MISE(\hat{\rho}(z; b)) = \int (\hat{\rho}(z; b) - \rho(z))^2 dz.$$

The difficulty is of course the lack of knowledge of $\rho(z)$. Although the choice of b is partly intuitive, (e.g. too large a value leads to an overly smooth estimate, and too small a value leads to an overly jagged estimate), it is difficult to judge the best value among reasonable values of b by mere qualitative observation. Although there are numerous methods of bandwidth selection, we choose to use the Least Squares Cross-Validation (LSCV) method described in [16] as a first estimate. We also found that by visual examination values of b in the range (0.13, 0.3) seem to provide reasonable results, and thus expect any optimization method to yield a value in this range. From [16], we optimize,

$$\begin{aligned} LSCV(b) &= \int_W \hat{\rho}(z; b)^2 dz - 2 \sum_{\mathbf{r}_i \in \Phi \cap W} \hat{\rho}(z_i; b) - k(0; b)/(Ac(z_i; b)) \\ &= \frac{1}{A^2} \sum_{\mathbf{r}_i \in \Phi \cap W} \sum_{\mathbf{r}_j \in \Phi \cap W} \int_W \frac{k_h(z - z_i)k_h(z - z_j)}{c_b(z)^2} dz - \frac{2}{A} \sum_{\mathbf{r}_i \in \Phi \cap W} \sum_{\mathbf{r}_j \in \Phi \cap W \setminus \mathbf{r}_i} \frac{k_b(z_i - z_j)}{c_b(z_i)}. \end{aligned}$$

With the Epanechnikov kernel, and ignoring edge effects for simplicity,

$$I(z_i; b) \equiv \int_W k_b(z - z_i)k_b(z)dz = \begin{cases} \frac{3}{160b} (32 - 40(z_i/b)^2 + 20|z_i/b|^3 - |z_i/b|^5) & |z_i| \leq 2b \\ 0 & |z_i| > 2b \end{cases}$$

$$LSCV(b) = \frac{1}{A} \left(\frac{3}{5b} \Phi(W) + \sum_{\mathbf{r}_i \neq \mathbf{r}_j} I(z_i - z_j; b) \right) - \frac{2}{A} \sum_{\mathbf{r}_i \neq \mathbf{r}_j} k_b(z_i - z_j)$$

A plot of $LSCV(b)$ versus b is shown in Figure 9. It can be seen that there exists several minima in each case, and the question is how to choose the “best” minima. In each case, the first minima, which is also the global minimum, is clearly too small leading to density estimates with unacceptably high variance. We found that the shallow local minimum at $b \approx 0.21$ worked best in practice. We additionally implemented the log-likelihood estimator described in [8] and found very similar results. It is unclear if there exists a method that possess a unique minimum in our case. There is also some evidence that spurious local minimizers of LSCV functionals tend to occur at smaller values than the optimal b , thus choosing the largest local minimizer seems a suitable strategy [19].

A.2 Bandwidth Selection for Estimation of the Pair Correlation Function

Similar to the estimation of a number density, the estimation of a pair correlation function bandwidth has an important effect upon the resulting estimator. From a theoretical perspective, it is easiest to analyze estimators of the form

$$\hat{g}(r) = \frac{1}{4\pi r^2 \bar{\gamma}_W(r) \rho^2} \sum_{\mathbf{r}_i \in \Phi \cap W} \sum_{\mathbf{r}_j \in \Phi \cap W \setminus \{\mathbf{r}_i\}} k_b(r - |\mathbf{r}_i - \mathbf{r}_j|)$$

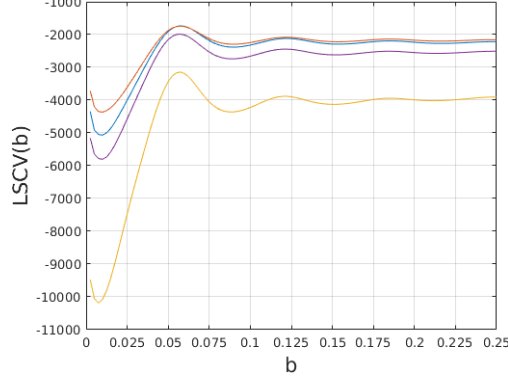


Figure 9: The Least Squares Cross Validation value for selected values of b over four data sets.

where $\bar{\gamma}_W(r)$ is known as the *isotropized set covariance* [41, 40]. It can be computed as the following integral over $\mathbf{t} \in \{\mathbf{s} \in \mathbb{R}^3 \mid |\mathbf{s}| = r\}$,

$$\bar{\gamma}_W(r) = \frac{1}{4\pi r^2} \int \nu(W \cap W_{\mathbf{t}}) d\mathbf{t}.$$

Although generally intractable to integrate analytically, for boxes, the integral can be computed:

$$\begin{aligned} \bar{\gamma}_W(r) &= \frac{1}{4\pi} \int \int \nu(W \cap W_{\mathbf{t}=(r,\theta,\phi)}) \sin \theta d\phi d\theta \\ &= \frac{2}{\pi} \int_0^{\pi/2} \int_0^{\pi/2} (l - r \sin \phi \cos \theta)(w - r \sin \phi \sin \theta)(h - r \cos \phi) \sin \theta d\theta d\phi \\ &= hlw - \frac{1}{2}(hl + lw + wh)r + \frac{2}{3\pi}(h + l + w)r^2 - \frac{1}{4\pi}r^3 \end{aligned}$$

for $r < \min(h, l, w)$. Then, following [35] and [40]

$$\text{Var}(\hat{g}(r)) \approx \frac{0.6g(r)}{4\pi b \rho^2 r^2 \bar{\gamma}_W(r)}.$$

It is noted in [40, §5] that this approximation is particularly accurate for hard-core processes. The bias can be computed as

$$\text{Bias}(\hat{g}(r)) = \left(\int k_b(r - r')g(r')dr' - g(r) \right)^2$$

Since the pair correlation function may exhibit a jump discontinuity near the hard-sphere radius, it is helpful to examine the integrated bias

$$\int \text{Bias}(\hat{g}(r))dr = \int \left(\int k_b(r - r')g(r')dr' - g(r) \right)^2 dr$$

Where $g(r)$ is twice differentiable, the bias and variance can be combined to obtain an approximation for the mean square error as a function of r and b ,

$$\mathbb{E} \left[(g(r) - \hat{g}(r; b))^2 \right] = \frac{0.6g(r)}{4\pi b \rho^2 r^2 \bar{\gamma}_W(r)} + \int k_b(r - r')r'^2 dr' g''(r).$$

Assuming $r > b$ since the hard-sphere diameter of bacteria is fairly large in comparison to the range over which we compute $g(r)$,

$$\mathbb{E} \left[(g(r) - \hat{g}(r; b))^2 \right] = \frac{0.6g(r)}{4\pi b \rho^2 r^2 \bar{\gamma}_W(r)} + \frac{1}{5}(b^2 + r^2)g''(r). \quad (11)$$

Table 2: Values of b determined through LSCV optimization are reported for intervals of r .

b	r_{min}	r_{max}
0.050	0.3	0.7
0.3700	0.7	1.6
0.2150	1.6	2.5
0.3960	2.5	5.0

Equation (11) can be minimized for each value of r to yield an analogous result to those typically derived in the case of probability density estimators (c.f. [33, 36]),

$$b(r) = \left(\frac{3}{8} \frac{g(r)}{\rho^2 r^2 \bar{\gamma}_W(r) g''(r)} \right)^{1/3}.$$

As is the case with density estimation, this expression is of limited usefulness since it depends on the unknown quantities, $g(r)$ and $g''(r)$. However, bandwidth selection methods, such as *least squares cross validation* (LSCV), and *biased cross validation* (BCV) [16, 47] can be applied to the integrated MSE to estimate an optimal value of b across the entire interval. For instance, the LSCV estimator for $g(r)$ can be formulated as in [15, Equation 4]. In addition, to the minimization method introduced in [15], we also employ a “binning” technique to estimate optimal values of b over disjoint portions of the overall interval of computation. The motivation for this adaptation is that the behavior of $g(r)$ is quite different near the hard-sphere radius in comparison to the asymptotic behavior for $g(r)$ as r grows. It seems sensible that different scale parameters should be applied in these different regimes. Thus, we employ LSCV functionals of the form

$$LSCV(h; [r_0, r_1]) = 4\pi \int_{r_0}^{r_1} \hat{g}(r; b)^2 r^2 dr - 2 \sum_{r_0 \leq |\mathbf{r}_i - \mathbf{r}_j| \leq r_1}^{\neq} \frac{\hat{g}^{-(\mathbf{r}_i, \mathbf{r}_j)}(|\mathbf{r}_i - \mathbf{r}_j|; h)}{\bar{\gamma}_W(|\mathbf{r}_i - \mathbf{r}_j|) \rho(\mathbf{r}_i) \rho(\mathbf{r}_j)}. \quad (12)$$

The symbol $\hat{g}^{-(\mathbf{r}_i, \mathbf{r}_j)}(r; h)$ indicates the computation of the pair correlation function with points \mathbf{r}_i and \mathbf{r}_j ignored. The expectation of the summation in Equation (12) is shown in [15] to converge in the limit of a large domain to

$$\int \hat{g}(r; h) g(r; h) 4\pi r^2 dr.$$

One can see from this the similarity to classical LSCV estimation of scale parameters for kernel density estimation [47].

In practice, we found that the summation of $\hat{g}^{-(\mathbf{r}_1, \mathbf{r}_2)}(\mathbf{r}_1, \mathbf{r}_2)$ was too expensive, leading to extremely lengthy computations. To alleviate this issue, we approximated $\hat{g}^{-(\mathbf{r}_1, \mathbf{r}_2)}(\mathbf{r}_1, \mathbf{r}_2)$ as

$$\hat{g}^{-(\mathbf{r}_1, \mathbf{r}_2)}(|\mathbf{r}_{12}|) \approx \mathcal{I}\hat{g}(|\mathbf{r}_{12}|) - \frac{2}{4\pi |\mathbf{r}_{12}|^2 \bar{\gamma}(|\mathbf{r}_{12}|)} \sum_{\mathbf{r}_i \neq \{\mathbf{r}_1, \mathbf{r}_2\}} (k_b(|\mathbf{r}_{12}| - |\mathbf{r}_{1i}|) + k_b(|\mathbf{r}_{12}| - |\mathbf{r}_{2i}|))$$

where $\mathcal{I}\hat{g}(\cdot)$ is the linear interpolant of $\hat{g}(\cdot)$ to some value (i.e. $|\mathbf{r}_{12}|$). The factor of 2 in the numerator of the second term is due arises since the terms involving $\mathbf{r}_{1i}, \mathbf{r}_{2i}, \mathbf{r}_{i1},$ and \mathbf{r}_{i2} must be subtracted from $\hat{g}(r)$. However, since $|\mathbf{r}_{ji}| = |\mathbf{r}_{ij}|$, there are only $\Phi(W)$ unique terms in the sum. With this fix, once $\hat{g}(r)$ is known, $\hat{g}^{-(\mathbf{r}_1, \mathbf{r}_2)}(|\mathbf{r}_{12}|)$ can be approximated in $\mathcal{O}(\Phi(W))$ computations as opposed to $\mathcal{O}(\Phi(W)^2)$ computations. As long as $\hat{g}(\cdot)$ is initially computed on a sufficiently dense set of points, the interpolant will be quite accurate. The resulting optimal values of b for different ranges of r are shown in Table 2. In practice, the value of $b(r)$ is assumed to be piecewise linear in r taking on the reported value in 2 at the midpoint of each interval. This prevents artificial discontinuities at the end points of the intervals over which b was estimated. Of course, if the estimator is accurate, one would expect such discontinuities to be small. Indeed, when $b(r)$ is a piecewise constant, discontinuities are difficult to discern by sight. We also use numerical integration to compute the relevant integrals in Equation (12).

One final issue with LSCV bandwidth selection is the presence of multiple minima. For the pair correlation function LSCV functional, spurious minima near $b = 0$ were observed. For the probability density estimation,

Figure 10: Variation in $LSCV(b; [0.6, 0.8])$ as b changes from 0.001 to 0.30. The presence of a spurious minimum near $b = 0$ is present, followed by a minimum near $b = 0.08$. The pair correlation function estimated over this interval for the two minima are shown. The pair correlation function estimate corresponding to the smaller value of b exhibits marked oscillations which we believe to be an indication of undersmoothing. In contrast, the larger minima yields a relatively smooth curve.

it has been suggested that spurious minima are usually less than the ideal bandwidth [19]. Thus, when multiple minima are present, we choose the minima that is largest over the range of values we consider for b . In Figure 10, we show the value of $LSCV(b; [0.6, 0.8])$ as b is varied.

An alternative approach to variable scale parameter estimation is use techniques such as that introduced in [1]. We believe such an approach would be effective as well.

A.3 Inhomogeneity of the Direct Pair Correlation Function in Nonstationary Processes

The motivation for using a transversely anisotropic pair correlation and direct correlation functions was attributed to properties of the Ornstein-Zernike equation. In this section we demonstrate why the Ornstein-Zernike equation implies a loss of translation invariance in the pair correlation function and direct correlation function when the density is variable.

Consider the inhomogeneous Ornstein-Zernike equation as shown in Equation (4). Let the two pairs of points $\{\mathbf{r}_1, \mathbf{r}_2\}$ and $\{\mathbf{r}'_1, \mathbf{r}'_2\}$ satisfy $\mathbf{r}_1 - \mathbf{r}_2 = \mathbf{r}'_1 - \mathbf{r}'_2 = \delta\mathbf{r}$, and assume that the pair correlation and direct correlation functions are translation invariant. Then, using the transformation $\mathbf{r}'_1 = \mathbf{r}_1 + \mathbf{x}$, $\mathbf{r}'_2 = \mathbf{r}_2 + \mathbf{x}$,

$$\begin{aligned} h(\mathbf{r}_1 - \mathbf{r}_2) &= c(\mathbf{r}_1 - \mathbf{r}_2) + \int \rho(\mathbf{r}_3) c(\mathbf{r}_1 - \mathbf{r}_3) h(\mathbf{r}_2 - \mathbf{r}_3) d\mathbf{r}_3 \\ - h(\mathbf{r}'_1 - \mathbf{r}'_2) &= c(\mathbf{r}'_1 - \mathbf{r}'_2) + \int \rho(\mathbf{r}_3) c(\mathbf{r}'_1 - \mathbf{r}_3) h(\mathbf{r}'_2 - \mathbf{r}_3) d\mathbf{r}_3 \\ \hline 0 &= \int \rho(\mathbf{r}_3) c(\mathbf{r}_1 - \mathbf{r}_3) h(\mathbf{r}_2 - \mathbf{r}_3) d\mathbf{r}_3 - \int \rho(\mathbf{r}_3) c(\mathbf{r}'_1 - \mathbf{r}_3) h(\mathbf{r}'_2 - \mathbf{r}_3) d\mathbf{r}_3 \end{aligned}$$

In order for this to be true for all translations, \mathbf{x} , it must be the case that $\rho(\mathbf{r}_3) = \text{const}$ almost everywhere. Thus, for a smoothly varying number density, it cannot be the case that $c(\mathbf{r}_1, \mathbf{r}_2)$ and $h(\mathbf{r}_1, \mathbf{r}_2)$ are both simultaneously translation invariant.